

Section 2

ADVANCED TECHNOLOGY DEVELOPMENTS

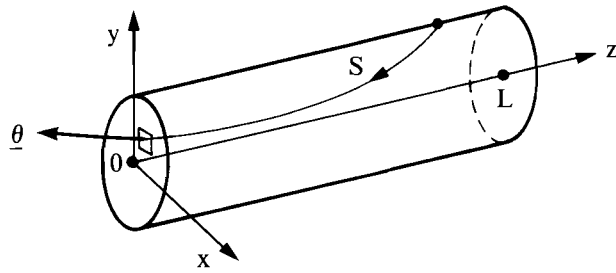
2.A CASER – A New Code for Calculating the X-Ray Laser Emission from Line-Focus Plasmas

X-ray laser gain due to collisional excitation has been observed from exploding-foil targets at Lawrence Livermore¹⁻³ and from solid targets at NRL.⁴ Crucial to the interpretation of both experiments is an understanding of x-ray refraction in the density profiles produced by line-focus irradiation.⁵ In this article we describe a new code, CASER (combine amplified spontaneous emission with refraction), which solves the radiation-transport equation along all relevant three-dimensional (3-D) x-ray trajectories through a line-focus plasma, and performs whatever integrations of the emerging flux over space, angle, time, and frequency are necessary in order to replicate experimental observations. The capabilities of the code are illustrated with reference to exploding selenium foils irradiated under the conditions of Livermore x-ray laser experiments.¹⁻³ While its present application is to x-ray laser experiments, the code has a broader potential application to a wide range of radiation-emission problems from multidimensional plasmas.

The general problem addressed by the code is illustrated in Fig. 38.17, with respect to a line-focus plasma that is approximately cylindrical in shape. Under the Livermore conditions, the plasma would be a few hundred microns in diameter and up to 4 cm long. In

Fig. 38.17

Geometry for determining the radiation emitted from a line-focus plasma. The total emission from the surface at $z = 0$ is the integral of the spectral intensity I_0 over space (x,y) , angle (θ_x, θ_y) , frequency, and time. I_0 is calculated by solving the radiation-transport equation (including a gain term) along each trajectory.



TC2413

order to determine the total energy (E_{tot}) radiated across the exit surface at $z = 0$, it is necessary to perform the following multidimensional integral:

$$E_{\text{tot}} = \int I_0(x, y, \theta_x, \theta_y, \nu, t, L) \cos\theta dx dy d\theta_x d\theta_y d\nu dt . \quad (1)$$

The integrand I_0 is the spectral intensity and has units $\text{ergs}\cdot\text{cm}^{-2}\cdot\text{srad}^{-1}\cdot\text{freq}^{-1}\cdot\text{sec}^{-1}$. It is assumed that all rays of interest emerge at small angles θ to the surface normal, so that $\cos\theta$ can be taken to equal unity. The integral is generally performed over the area of the exit surface in the x - y plane as shown in the figure. However, it is sometimes necessary to increase the area of integration to include contributions from rays emerging from the curved edge of the plasma. The integral over angle (θ_x, θ_y) is dominated by the contributions of rays whose trajectories encompass all or most of the length of the plasma in the z direction. The quantity θ_x is defined to be the cosine of the angle between the direction of the emerging ray and the x axis. For small angles from the surface normal, θ_x is the angular deviation of the emerging ray from the z axis, measured in the x direction.

Integration over the spectral profile $\Psi(\nu)$ is necessary because different portions of the spectrum see different gain in the plasma, and integration over time is required for all except time-resolved diagnostics. The spectral intensity I_0 at the exit surface ($z = 0$) is the solution of the radiation transfer equation

$$\frac{dI}{ds} = gI + \sigma \quad (2)$$

along the trajectory, integrated through a plasma of length L . (Corrections to this equation due to a spatially varying refractive index⁶ are negligible in our application since the refractive index $\mu \approx 1$.)

In Eq. (2), the term σ represents spontaneous emission and a positive g signifies gain. (For most plasmas, g is negative and represents the opacity, corrected for stimulated emission.) For a spectral line, we can write $g(\nu) = g_0 \Psi(\nu - \nu_0)$, where Ψ gives the line shape [normalized so that $\Psi(0) = 1$] and g_0 gives the line-center gain. For the Livermore x-ray laser, we assume a Doppler line shape with width proportional to the square root of the ion temperature. We assume that g and σ share the same line shape.

The trajectories are calculated by integrating the 3-D ray equation,⁷ simplified for the case of current interest where $\mu \approx 1$ and the path length $s \approx z$:

$$\begin{aligned} \frac{d}{dz}(x, y) &= (\theta_x, \theta_y) \\ \frac{d}{dz}(\theta_x, \theta_y) &= \left(\frac{\partial \mu}{\partial x}, \frac{\partial \mu}{\partial y} \right) \\ \mu &= (1 - n_e/n_c)^{1/2}, \end{aligned} \quad (3)$$

where n_e is the electron-number density and n_c is the critical electron-number density corresponding to the x-ray wavelength ($2.8 \times 10^{24} \text{ cm}^{-3}$ for 200 Å). Each trajectory is calculated backwards starting from the emerging point (x, y) and direction (θ_x, θ_y) , and terminating at $z = L$ unless the ray first enters across the curved boundary (as occurs in Fig. 38.17 at point P). If it is desired, the radiation-transport equation can then be integrated forward along the trajectory (i.e., in the direction of decreasing z) for each frequency in the spectrum to include effects due to a spatially varying line shape. However, in some cases it is reasonable to assume that σ/g is independent of space and frequency; some computational time can then be saved by using the analytic solution⁵ to Eq. (2) at the line center:

$$I_0 = \frac{\sigma}{g} (e^G - 1), \quad (4)$$

where

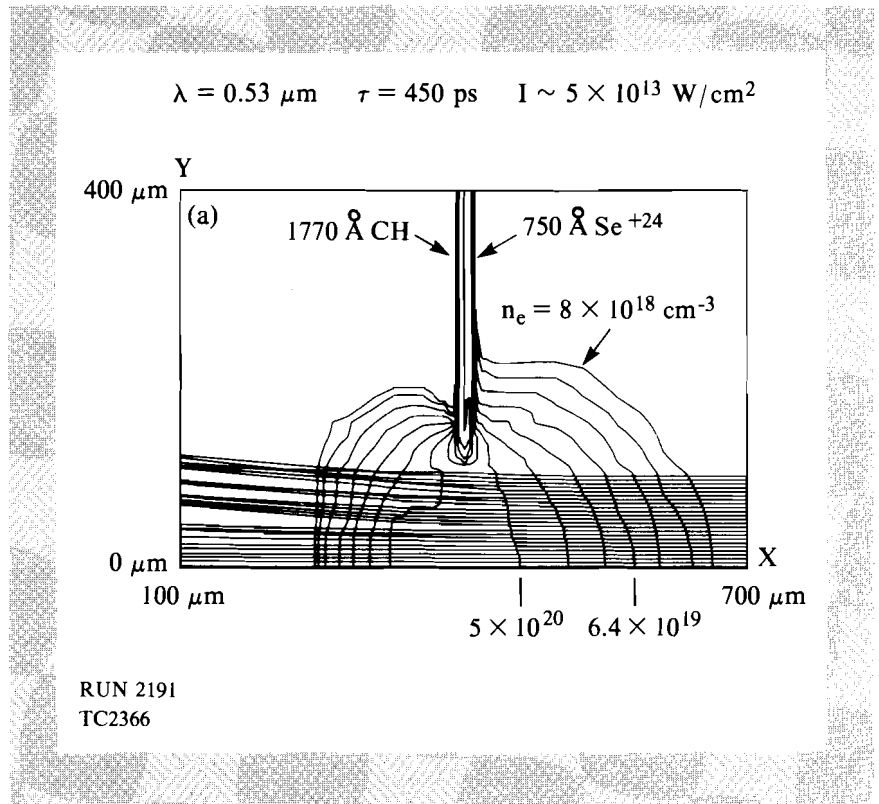
$$G = \int g dz. \quad (5)$$

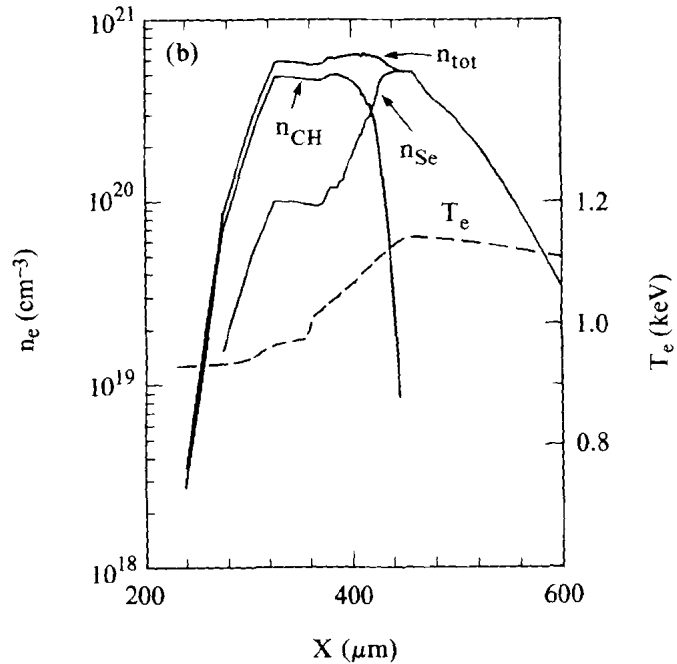
The frequency dependence of I_0 can then be easily found since G has the same line shape as g .

It should be noted that CASER does not calculate the quantities n_e , g , and σ . These need to be supplied from hydrodynamic and atomic-physics models. In the work presented here, n_e is obtained from a simulation using the two-dimensional (2-D) hydrodynamics code *SAGE*, and g and σ from an ad hoc model.

In order to illustrate its features, the code has been used as a postprocessor to a 2-D *SAGE* simulation of an exploding selenium foil, under conditions representative of the Livermore experiment reported in Refs. 1 and 2. The experiment (750 Å Se on 1500 Å of Formvar irradiated at 5×10^{13} W/cm²) was modeled using 750 Å of Se⁺²⁴ (perfect gas) on the CH thickness (1770 Å) equivalent to 1500 Å of Formvar. Representative density contours at the peak of the (optical) laser pulse are shown in Fig. 38.18(a). The laser is incident from the right and has just burned through the foil; the plasma extent is therefore greater on the right (selenium) side of the figure. The plasma is assumed symmetrical about the plane $y = 0$. Lineouts of electron density and temperature in this plane are shown in Fig. 38.18(b), including separate profiles for the CH and the Se. A problem with the current treatment of multiple materials in the Eulerian code *SAGE* is that separate equations are solved for each of the two densities, leading to some numerical diffusion. (The code contains no physical model for diffusion or mixing. The question of whether inter-material diffusion occurs to a significant extent in the experiment is not addressed here.) The extent of the numerical diffusion may appear to be exaggerated because the densities are plotted on a logarithmic scale; however, it is clear that the boundary between the two materials occurs just to the right of center, about 20 μm to the selenium side. This is consistent with the fact that, although the target initially contains 10% more selenium electrons (assuming neon-like ionization to Se⁺²⁴), some of the selenium is ablated early in the interaction. In a comparison calculation using two-sided irradiation, the boundary appears a little to the left of center.

Fig. 38.18(a)
SAGE simulation of an exploding CH/Se foil, for conditions corresponding to Livermore x-ray laser experiments. The foil is irradiated in line-focus geometry by a single beam, incident from the right in a 450-ps pulse of 532-nm light at 5×10^{13} W/cm². Just after the laser burns through the foil a region of small density gradient is established near the center, allowing propagation of x rays through long distances in the z direction.





RUN 2191
TC2400

Fig. 38.18(b)
Lineouts of electron density and temperature along the x axis of Fig. 38.18(a), including individual densities of the CH and selenium components. In spite of some numerical diffusion of the two components into each other, the boundary between the two is approximately in the center of the profile.

In the CASER calculations presented here, the x rays are bent according to the gradients of total electron density n_e . A very simple ad hoc formula is used for the intrinsic line-center gain g_0 :

$$g_0 = 1.25 \times 10^{-20} n_{Se}; \tag{6}$$

whenever the following three conditions are all satisfied: selenium must be the dominant material ($n_{Se} > n_{CH}$), the inversion must not be destroyed by collisions ($n_e < 10^{21} \text{ cm}^{-3}$), and the plasma must be sufficiently hot to be in the neon-like state ($T_e \geq 300 \text{ eV}$). If any of these conditions are not satisfied, g_0 is taken to be zero.

The exact position of the plastic/selenium interface is important because optimum x-ray lasing from long plasmas requires that the intrinsic gain be high in the central region of gentle electron density gradient. For the case of one-sided irradiation presented here, this requirement is clearly not met because the material in the center is plastic. For the case of two-sided irradiation the requirement is met, because the material in the center is selenium and the gain (assumed proportional to selenium density) is maximum there. This difference may partially explain the following experimental observation:

- (a) In the original NOVETTE experiments,¹ the signal up to a plasma length of 1 cm grew exponentially and was not greatly different for one- or two-sided irradiation;
- (b) In the same experiments,¹ the rate of growth of signal for one-sided irradiation fell off between 1 cm and 2 cm;
- (c) In later experiments on NOVA³ with two-sided irradiation, exponential growth was maintained up to 4 cm.

However, the actual spatial and temporal dependence of the intrinsic gain g_0 is far from certain. It has been inferred from experimental observations that g_0 is low in the center for at least a significant portion of the disassembly time of the foil.^{3,5}

Fig. 38.19

Ray trajectories used to perform the spatial integration (over x and y) at one specific time (the peak of the pulse) and in one direction ($\theta_x = 10$ mrad, $\theta_y = 0$). Trajectories with values of y greater than $20 \mu\text{m}$ are omitted for clarity. Gain exists in the plasma on the selenium side only ($x \geq 420 \mu\text{m}$), and peaks at $x \approx 450 \mu\text{m}$. The integration algorithm selects those rays providing the dominant contributions.

In the integral of Eq. (1), the code typically integrates over all points x and y emerging in a specified direction. It can alternatively integrate over all angles θ_x and θ_y emerging from a specified point. In either case, just a small subset of possible rays provides the dominant contribution to the integral. This problem was recognized by London⁵; in order to obtain a convergent integral within reasonable computation time, it is necessary for CASER to select the most important rays automatically. How this is achieved is illustrated in Figs. 38.19 and 38.20.

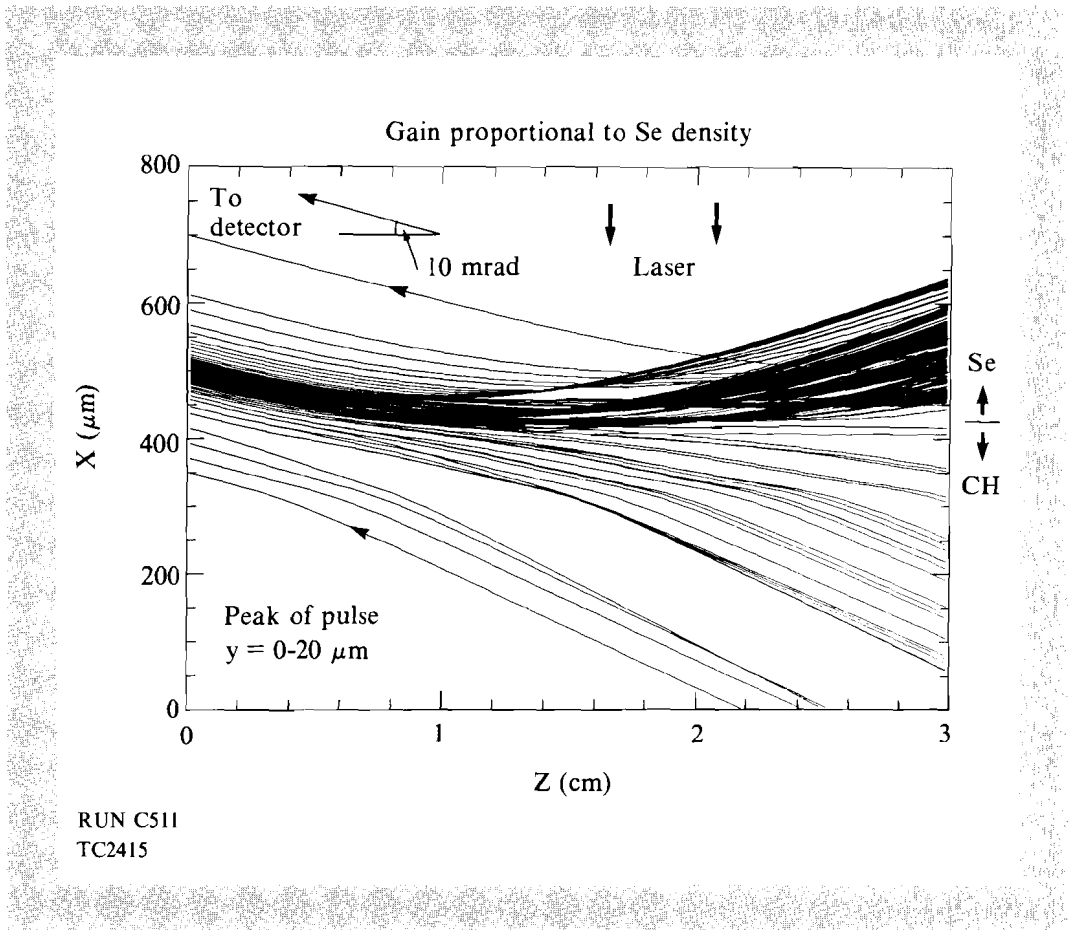


Figure 38.19 shows ray trajectories used in the integration through the profile of Fig. 38.18(a) to obtain the signal seen by a detector placed at 10 mrad to the z axis, for a plasma of 3-cm length. [Strictly speaking, it is the projection of the trajectories in the (x,z) plane that is shown.] Rays travel to the left, and emerge from the plasma at $z = 0$ with an angle θ_x of 10 mrad. The top half of the figure ($y \geq 400 \mu\text{m}$) is selenium and contains all the gain. For clarity, the figure shows just those trajectories emerging with $0 \leq y \leq 20 \mu\text{m}$. The dominant rays emerge across a small portion of the exit surface at $x \approx 500 \mu\text{m}$, having experienced a turning point around $x = 450 \mu\text{m}$ about halfway along the line focus. If gain were permitted on the CH side, we would observe a more symmetric clustering on the right-hand edge of the figure; i.e., at $z = 3 \text{ cm}$, the dominant rays would start with $200 \leq x \leq 600 \mu\text{m}$ rather than with $400 \leq x \leq 600 \mu\text{m}$.

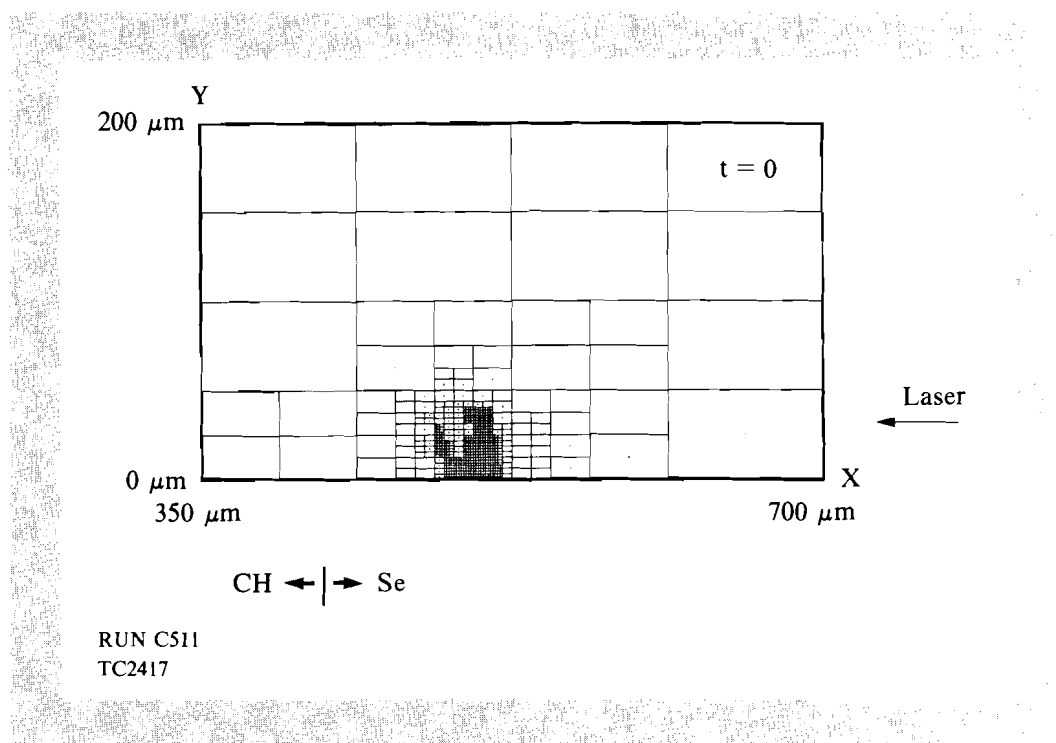


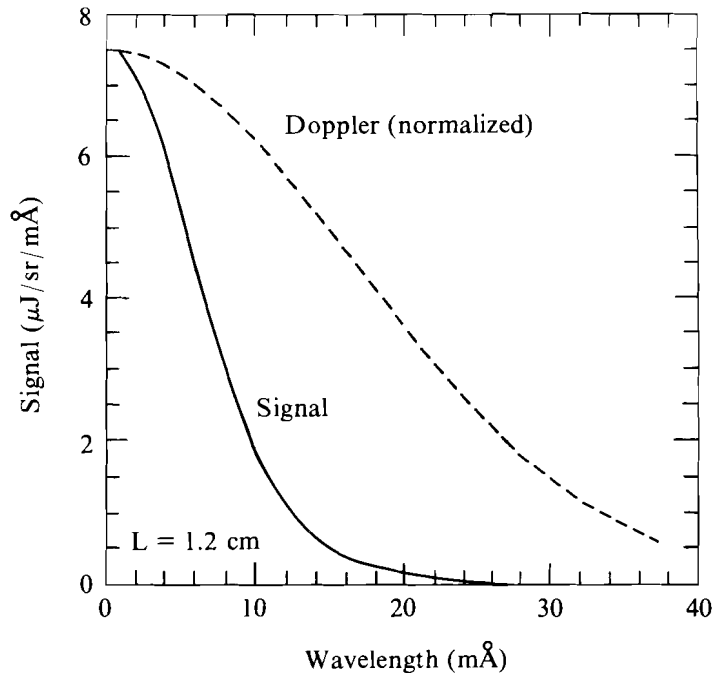
Fig. 38.20

Subdivision of the (x,y) plane corresponding to the trajectories of Fig. 38.19. Cells with large percentage contributions to the total integral have been successively subdivided. The dense portion indicates the small region responsible for the bulk of the gain.

Figure 38.20 shows how the (x,y) plane is successively subdivided during the integration. Cells with large fractional contributions to the total integral are subdivided into four smaller cells, whose contributions are then recalculated. Simpson's Rule in two dimensions is applied to each cell, necessitating trajectory computations at each cell center and corner. In order to avoid redundant trajectory computations, the integrand is actually a 2-D matrix of spectral intensities I_0 corresponding to various frequencies and plasma lengths, with the subdivision pattern illustrated in Fig. 38.20 determined by the

largest element in the matrix (the line-center signal from the longest plasma length). The algorithm also necessarily includes means to ensure that if the region to one side of an interface is subdivided more than once, then the cell to the other side is subdivided regardless of its current contribution. The algorithm may be thought of as a numerical analog to a saddle-point integration. The large memory of the LLE Cyber 990 and its vector capability enable the integration to be performed efficiently.

The space- and time-integrated spectrum from a plasma of 1.2-cm length, as used in Ref. 1, is shown in Fig. 38.21 for a viewing angle θ_x of 7 mrad (with $\theta_y = 0$). The intrinsic (Doppler) profile, corresponding to the constant $T_i = 500$ eV used for this calculation, is shown for comparison. (For this plasma, where T_i varies much slower spatially than g_0 , a constant value of T_i is a reasonable approximation.) An inspection of the FWHM's of these two profiles indicates a narrowing by a factor of 2.9. This narrowing occurs because the line center experiences the strongest amplification. For an amplifier with a gain-length product G , it is easy to show that the narrowing factor is $G^{1/2}$ in the limit of large G .⁸ If we were to define an "average" intrinsic gain \bar{g} by equating $(\bar{g}L)^{1/2}$ to 2.9, we would find $\bar{g} = 7.0 \text{ cm}^{-1}$, a value close to the experimentally inferred gain¹ of 5–6 cm^{-1} . However, this procedure is not strictly justified since the spectrum of Fig. 38.21 does not correspond to a single intrinsic gain but is an integral over space and time.



RUN C511
TC2418

Fig. 38.21
Spectrum for a plasma of length 1.2 cm, integrated over space and time. Narrowing of the signal relative to the Doppler line profile intrinsic to the plasma is an indication of gain.

The most dramatic indication of x-ray lasing is seen when the signal, integrated over time, space, and wavelength, is plotted against plasma length (see Fig. 38.22). Here, the experimental points reported by Matthews *et al.* [Ref. 1, Fig. 4(a), two-sided illumination] are superposed for comparison. The calculation is normalized at 1.2 cm by an appropriate choice of σ/g . The factor 1.25×10^{-20} of Eq. (6) was chosen in order to provide a good fit to the data; a substantially poorer fit was obtained with this factor equal to 1.0×10^{-20} . The dashed and dotted curves of Fig. 38.22 are fits of the form $\exp(\bar{g}L) \cdot (\bar{g}L)^{-1/2}$ used by Matthews *et al.*,¹ with $\bar{g} = 5$ and 6 cm^{-1} respectively. The square-root term in this formula takes into account spectral narrowing; its origin is easy to understand since the integral over frequency is approximately the line-center gain times the width, and the width scales as $(\bar{g}L)^{-1/2}$ in the limit of large $\bar{g}L$. However, use of this formula is not justified since similar square-root terms could arise

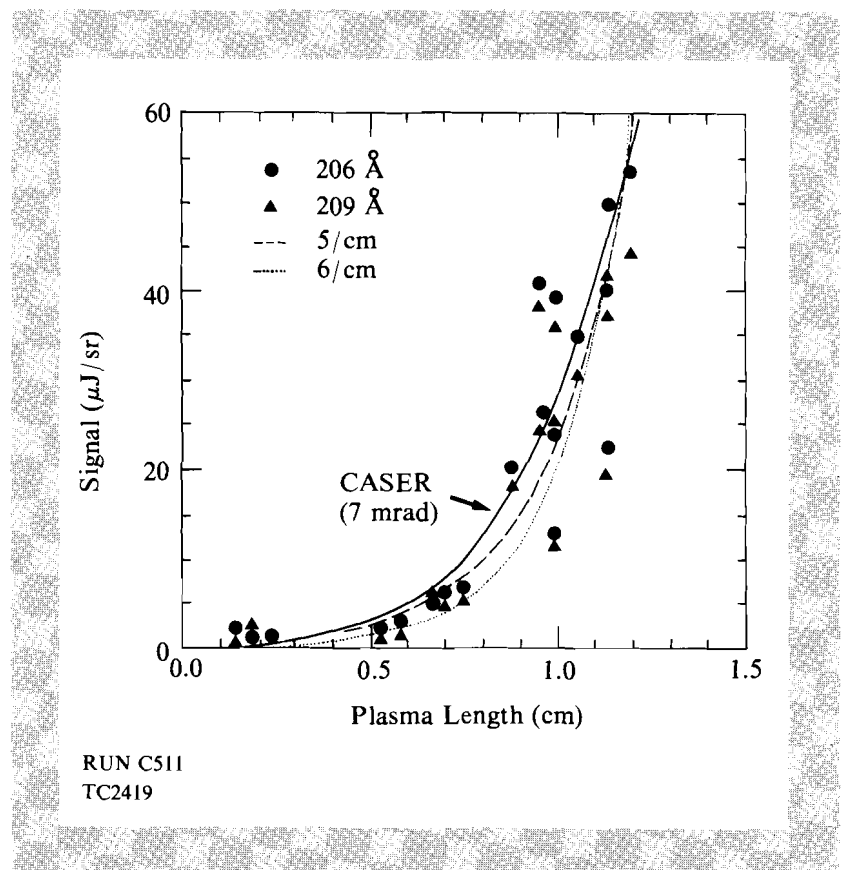


Fig. 38.22
Dependence of the integrated x-ray signal on plasma length. Simulation results (solid line) are compared with Livermore data for two lasing transitions. The dashed and dotted lines are fits to the Livermore data of form $\exp(G)/G^{1/2}$.

from the integrals over time and two spatial dimensions assuming (as is reasonable) that the gain is not uniform in space and time. Also, of course, the formula ignores refraction. A calculation such as is presented here is necessary to relate the gain inferred from observations integrated over time, space, and wavelength to the intrinsic gain in the plasma.

The angular dependence of the calculated signal, with respect to the angle θ_x and for the greatest length used in Fig. 38.22 (i.e., 1.2 cm),

is shown in Fig. 38.23. The signal is seen to be quite peaked off-normal and strongly increasing from 0 to 10 mrad. This is due primarily to the selenium density (and therefore the intrinsic gain) falling off in the center of the plasma. A very similar curve to Fig. 38.23 was reported in Fig. 8 of Ref. 3, albeit for a 3-cm plasma and two-sided irradiation. It is possible that the large scatter in the experimental data seen in Fig. 38.22 for lengths around 1 cm is related to the strong dependence of signal on detector angle.

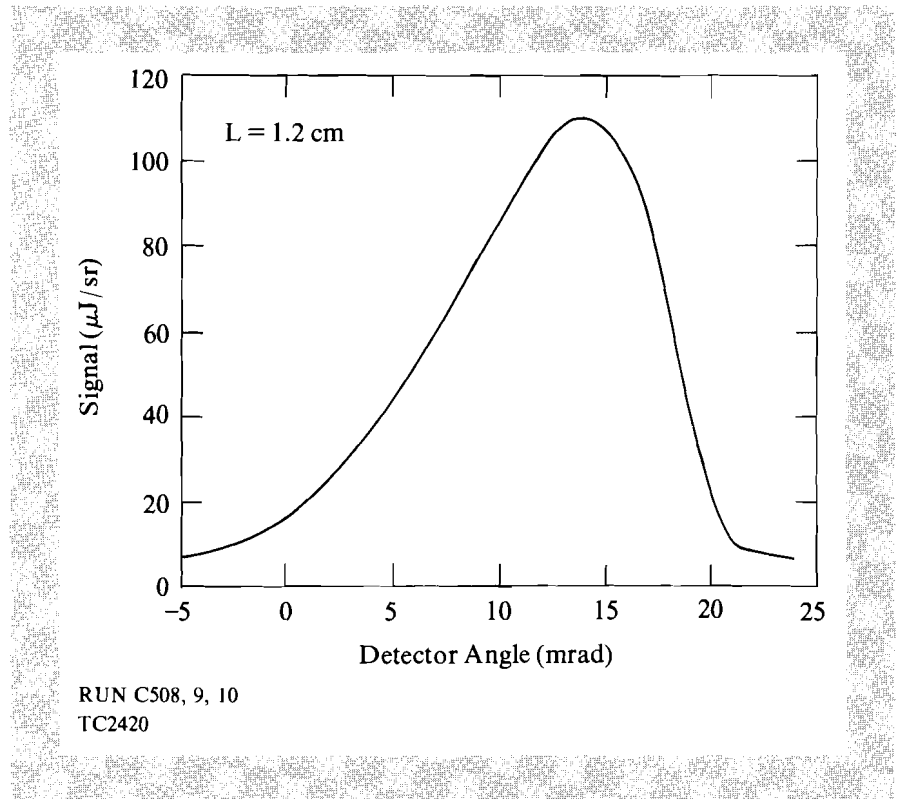


Fig. 38.23

Dependence of the integrated x-ray laser signal on the viewing angle θ_x of the detector, for a 1.2-cm plasma. The peak at $\theta_x = 13$ mrad is a consequence of the deficit of selenium in the center of the plasma.

Finally, the time evolution of the x-ray laser signal is shown in Fig. 38.24 for two viewing angles, $\theta_x = 0$ and 7 mrad. As discussed, the signal at 7 mrad is the stronger signal. Both signals occur just before the peak of the driving laser pulse, with the 7-mrad signal peaking slightly earlier, qualitatively in agreement with Fig. 1 of Ref. 9. The FWHM's are 190 ps and 150 ps, respectively, somewhat less than the 290 ps observed in Fig. 3(a) of Ref. 1 for a 1-cm target displaying "moderate amplification," but consistent with the observation of Ref. 1 that the pulse width decreases with increased amplification.

In summary, the code CASER should prove useful in predicting experimental observations of x-ray lasing, given models of intrinsic gain within line-focus plasmas. The primary purpose of this article has

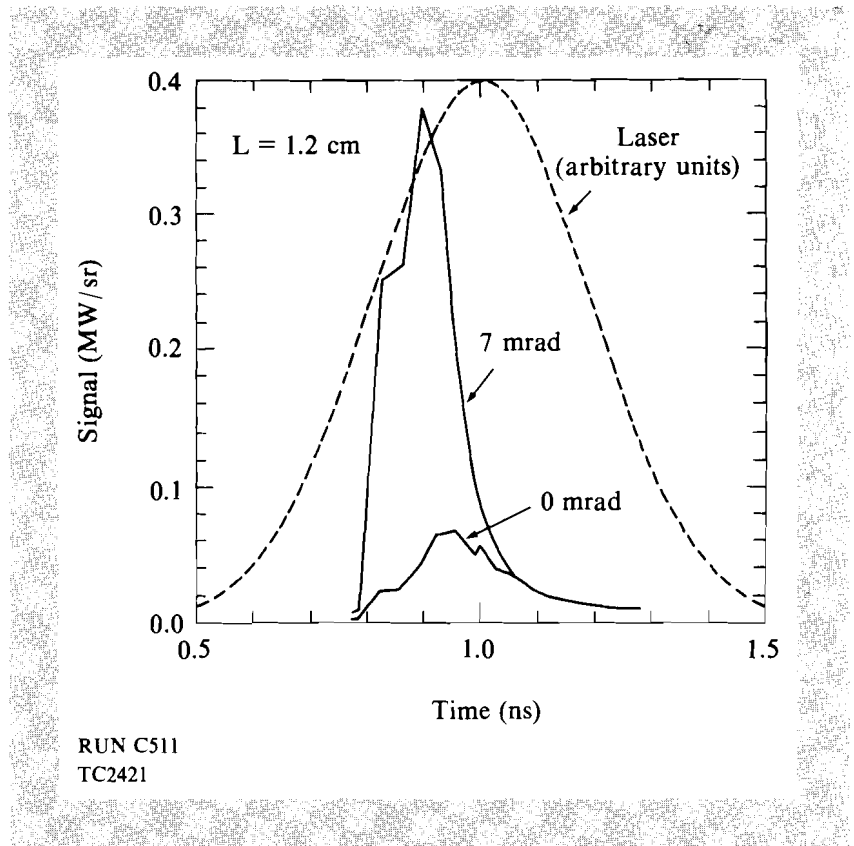


Fig. 38.24
Streaked x-ray laser emission from a 1.2-cm plasma, as viewed from two different directions. The 7-mrad signal emerges slightly earlier in time when refraction is more important. Later in time, when the density gradients have relaxed, there is no significant difference.

been to illustrate some of the capabilities of CASER. A more thorough analysis of the large data base of Livermore and NRL experiments is in progress, and depends in part on using a more realistic gain model. Given a reasonable gain model, the code will enable proposed new configurations for x-ray laser targets¹⁰ to be evaluated and optimized with respect to refraction. This could permit useful gain to be obtained from lasers of modest energy.

ACKNOWLEDGMENT

This work was supported by the Laser Fusion Feasibility Project at the Laboratory for Laser Energetics, which has the following sponsors: Empire State Electric Energy Research Corporation, New York State Energy Research and Development Authority, Ontario Hydro, and the University of Rochester. Such support does not imply endorsement of the content by any of the above parties.

REFERENCES

1. D. L. Matthews *et al.*, *Phys. Rev. Lett.* **54**, 110 (1985).
2. M. D. Rosen *et al.*, *Phys. Rev. Lett.* **54**, 106 (1985).
3. D. Matthews *et al.*, *J. Opt. Soc. Am. B* **4**, 575 (1987).
4. T. N. Lee, E. A. McLean, and R. C. Elton, *Phys. Rev. Lett.* **59**, 1185 (1987).
5. R. A. London, *Phys. Fluids* **31**, 184 (1988).